Available online at www.sciencedirect.com
SCIENCE DIRECT®
International Journal of Heat and Mass Transfer 49 (2006) 2190–2206
International Journal of HEAT and MASS TRANSFER
www.elsevier.com/locate/ijhmt

Mixed convection in a square vented enclosure filled with a porous medium

Shohel Mahmud [a,*], Ioan Pop [b]

[a] Department of Mechanical Engineering, University of Waterloo, 200 University Ave West, ON, Canada N2L3G1
[b] Faculty of Mathematics, University of Cluj, R-3400 Cluj, CP 253, Romania

Received 19 August 2005; received in revised form 23 November 2005
Available online 2 March 2006

Abstract

Steady mixed convection flow in a vented enclosure with an isothermal vertical wall and filled with a fluid-saturated porous medium is investigated numerically. The forced flow conditions are imposed by providing an inlet at the bottom surface, and a vent at the top, facing the inlet. The nature and the basic characteristics of the mixed aiding as well as mixed opposing flows that arise are investigated using the Darcy law model. The governing parameters are the Rayleigh number, Péclet number, and the width of the inlet as a fraction of the height of the square enclosure. These parameters are varied over wide ranges and their effect on the heat transfer characteristics is studied in detail.

Keywords: Mixed convection; Square vented enclosure; Porous medium; Numerical results

1. Introduction

Convective heat transfer in saturated porous media has received considerable attention during the past several decades because of its wide range of applications. These applications include packed bed reactors, porous insulation, beds of fossil fuels, nuclear waste disposal, usage of porous conical bearings in lubrication technology, fibrous insulation systems, grain storage, food processing, energy efficient drying processes, geophysics, and energy related engineering problems. The fundamental nature and the growing volume of works in this area are amply documented in the books by Nield and Bejan [1], Ingham and Pop [2–4], Vafai [5,6], Pop and Ingham [7], Bejan and Kraus [8], Ingham et al. [9] and Bejan et al. [10], and the review articles by Hadim and Vafai [11], and Vafai and Hadim [12]. Convective flow inside a square and/or rectangular cavity filled with a fluid-saturated porous medium has been studied extensively in the past due to its applications in many engineering and geophysical systems, including nuclear and electronic equipment cooling, post-accidental heat removal in nuclear reactors, solar power collectors, cooling of radioactive waste containers, to name just a few (see [13]). A rich variety of important analytical, numerical, and experimental results have been published on this topic and they are important to better understand the thermal convection inside porous cavities. The technical issues of mixed convection flow in porous media have been concerned mainly with situations in which buoyancy effects are substantial, if not entirely dominant. This leads to an immediate identification of the flow regimes of interest.

Attention will be focused in this paper on a new problem of steady mixed convection inside a square vented cavity filled with a fluid-saturated porous medium, with one of the vertical wall being at constant temperature and the remaining walls being perfectly insulated (adiabatic). By providing an inlet and an exit vent, forced convection conditions can be imposed inside the porous enclosure. The imposed forced flow may aid the natural convection flow

* Corresponding author. Tel.: +1 519 888 4567x3885; fax: +1 519 888 6197.
E-mail address: smahmud@uwaterloo.ca (S. Mahmud).

0017-9310/$ - see front matter © 2006 Elsevier Ltd. All rights reserved.
doi:10.1016/j.ijheatmasstransfer.2005.11.022

Nomenclature

D	width of the inlet, and the vent, m
$\mathbf{g}$	gravitational acceleration, m s^{-2}
H	cavity height, m
K	permeability of the porous medium, m^2
Nu	local Nusselt number
Nu_{av}	average Nusselt number
Pe	Péclet number
Ra	Rayleigh number for the porous medium
t	time, s
T	temperature, °C
T_0	temperature of the throughflow at the inlet, °C
T_w	temperature of the isothermal vertical surface, °C
$\vec{\mathbf{v}}$	velocity vector, m s^{-1}
u, v	velocity components along x- and y-axes, respectively, m s^{-1}
U, V	dimensionless velocity components along x- and y-axes, respectively
V_0	absolute value of the velocity of the forced flow at the inlet, m s^{-1}
x, y	Cartesian coordinates, m
X, Y	dimensionless Cartesian coordinates
Greek symbols	
α_m	effective thermal diffusivity, m^2 s^{-1}
β	coefficient of thermal expansion, K^{-1}
θ	dimensionless temperature
σ	ratio of composite material heat capacity to convective fluid heat capacity
τ	dimensionless time
υ	kinematic viscosity, m^2 s^{-1}
ψ	dimensionless stream function

(aiding mixed convection flow), or oppose it (opposing mixed convection flow), depending on the direction of the forced flow. Conversely, the buoyancy may aid or oppose the forced flow, depending on whether the surface temperature is higher or lower than the temperature of the incoming forced fluid flow. Also this type of geometry is frequently encountered in micro-electronic devices. Two examples are presented in Fig. 1a (a vented enclosure packed with micro-pinfin) and Fig. 1b (a vented enclosure packed with micro-sphere), respectively. It is worth mentioning to this end that for a viscous and incompressible fluid (non-porous medium) the analogous problem has been recently studied by Angirasa [14]. Angirasa [14] dealt with the similar vented enclosure without porous media. Other works on mixed convection in porous media are also available [15–23].

2. Basic equations

Consider a square enclosure filled with a fluid-saturated porous medium with the left vertical wall at the constant temperature, T_w, and the other walls adiabatic. Mixed convection conditions arise due to the provision of a forced flow through a slot at the bottom edge of the vertical surface, and a vent at the top edge for outflow, as shown in Fig. 1c. It is assumed that D is the width of the inlet and the vent. Buoyancy effects are induced due to the difference in temperature between the left vertical wall, T_w, and the throughstream temperature, T_0, which has a constant velocity, V_0, at the inlet of the enclosure. The inlet forced flow is fixed at the bottom and the temperature difference $(T_w - T_0)$ is considered to be either positive (aiding flow) or negative (opposing flow), respectively. In the porous media, the following assumptions are made: the fluid and the porous medium are in local thermal equilibrium; the properties of the fluid and the porous media are constant; the viscous drag and inertia terms of the momentum equations are negligible, and the Darcy and Boussinesq approximations are valid.

Under these assumptions, the conservation equation for mass becomes

$$\frac{\partial u}{\partial x} + \frac{\partial v}{\partial y} = 0. \tag{1}$$

Using the assumptions, the momentum flow inside the enclosure can be modelled by the Darcy flow model [1] which constructs a relationship between the flow velocity at a certain direction to the pressure gradient in that direction; that is,

$$\mathbf{v} = \frac{K}{\mu}(-\nabla p + \rho \mathbf{g}), \tag{2}$$

in vector form where, $\mathbf{v}$, K, μ, p, and $\mathbf{g}$ are the velocity vector, permeability, viscosity, pressure, and gravity vector, respectively. The permeability K is an empirical constant which may define a length scale squared of pores. The Darcy flow model is valid in circumstances where the order of magnitude of the *local pore Reynolds number*, based on the local volume averaged speed $(|\mathbf{v}|^{1/2})$ and $K^{1/2}$, is smaller than 1. Darcy's law also neglects the effects of a solid boundary or the inertial forces on fluid flow. These effects are expected to become more significant near the boundary and in high-porosity media, thus causing the application of Darcy's law invalid. Taking the '**curl**' on the both sides of Eq. (2) using the assumptions, $\mathbf{v} = u\mathbf{i} + v\mathbf{j} + 0\mathbf{k}$ and $\mathbf{g} = 0\mathbf{i} + g_y\mathbf{j} + 0\mathbf{k}$, results in the following momentum equation:

$$\frac{\partial u}{\partial y} - \frac{\partial v}{\partial x} = -\frac{g\beta K}{\upsilon}\frac{\partial T}{\partial x}, \tag{3}$$

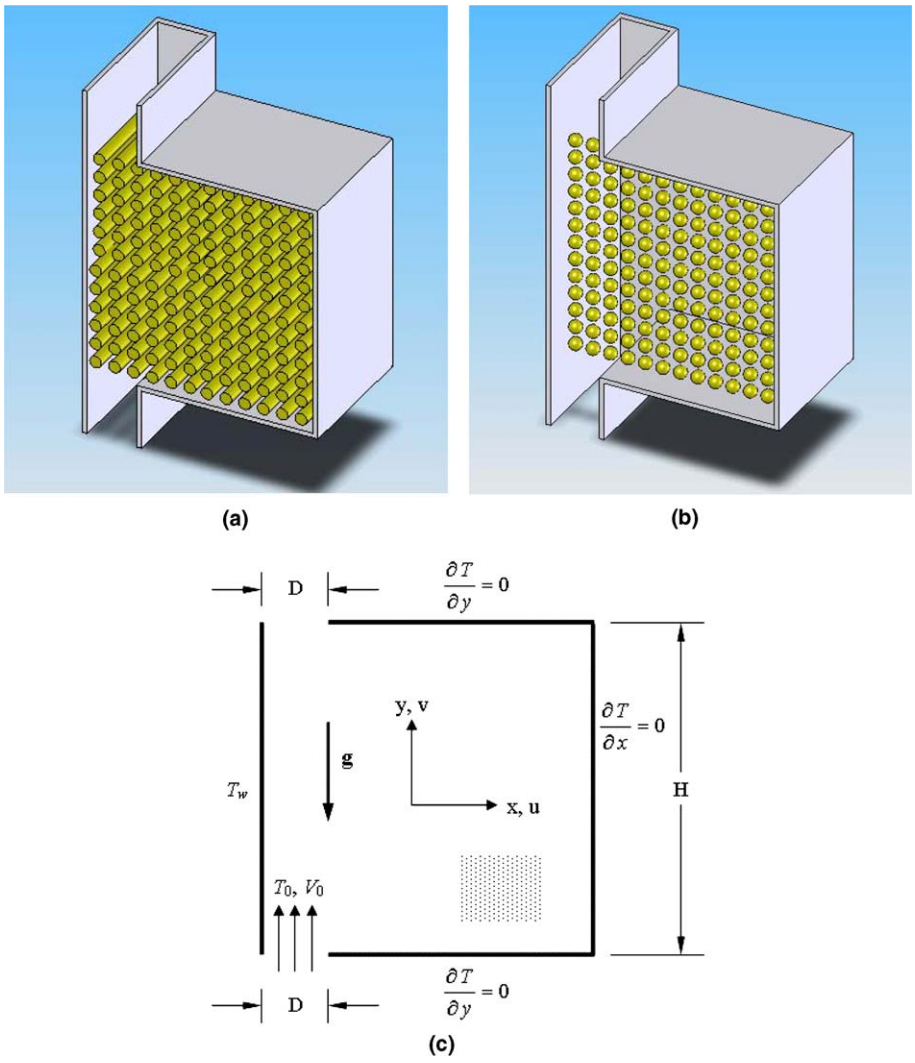

Fig. 1. (a) An enclosure packed with micro-pinfin, (b) an enclosure packed with micro-sphere, and (c) physical model and the coordinate system.

where $g = g_y$. Eq. (3) has no pressure term. Finally, the energy equation, according to Nield and Bejan [1], is

$$\sigma\frac{\partial T}{\partial t}+u\frac{\partial T}{\partial x}+v\frac{\partial T}{\partial y}=\alpha_m\left(\frac{\partial^2 T}{\partial x^2}+\frac{\partial^2 T}{\partial y^2}\right), \tag{4}$$

where x, y are the Cartesian coordinates measured in the horizontal and vertical directions, u, v are the velocity components along x- and y-axes, and T is the fluid temperature, respectively. The physical meaning of the other quantities are mentioned in Nomenclature.

We introduce the following non-dimensional variables:

$$X=\frac{x}{H},\quad Y=\frac{y}{H},\quad \tau=\frac{V_0 t}{\sigma H},\quad U=\frac{u}{V_0},$$
$$U=\frac{v}{V_0},\quad \theta=\frac{T-T_0}{T_w-T_0} \tag{5}$$

and define the dimensionless stream function, ψ, in the usual way as

$$U=\frac{\partial\psi}{\partial Y},\quad V=-\frac{\partial\psi}{\partial X}. \tag{6}$$

Substituting Eqs. (5) and (6) into Eqs. (3) and (4), the following non-dimensional equations are obtained:

$$\frac{\partial^2\psi}{\partial X^2}+\frac{\partial^2\psi}{\partial Y^2}=-\frac{Ra}{Pe}\frac{\partial\theta}{\partial X} \tag{7}$$

and

$$\frac{\partial\theta}{\partial\tau}+\frac{\partial\psi}{\partial Y}\frac{\partial\theta}{\partial X}-\frac{\partial\psi}{\partial X}\frac{\partial\theta}{\partial Y}=\frac{1}{Pe}\left(\frac{\partial^2\theta}{\partial X^2}+\frac{\partial^2\theta}{\partial Y^2}\right), \tag{8}$$

where Ra and Pe are the Rayleigh and Péclet numbers for a porous medium which are defined by

$$Ra=\frac{gK\beta(T_w-T_0)H}{\alpha_m\upsilon},\quad Pe=\frac{V_0 H}{\alpha_m}. \tag{9}$$

It is worth mentioning that the Rayleigh number may be either positive, $T_w > T_0$ (aiding flow) or negative, $T_w < T_0$ (opposing flow), respectively.

The numerical simulation is carried out in the time domain but the final steady-state flow and heat transfer characteristics will be presented only in the subsequent sections. The boundary conditions of Eqs. (7) and (8) are

Left isothermal wall:

$$\psi = 0,\ \ \theta = 1 \quad \text{on } X = 0,\ \ 0 \leqslant Y \leqslant 1, \tag{10a}$$

Inlet:

$$\psi = -X,\ \ \theta = 0 \quad \text{on } Y = 0,\ \ 0 \leqslant X \leqslant D/H, \tag{10b}$$

Bottom adiabatic wall:

$$\psi = -D/H,\ \ \partial\theta/\partial Y = 0 \quad \text{on } Y = 0,\ \ D/H < X \leqslant 1, \tag{10c}$$

Right adiabatic wall:

$$\psi = -D/H,\ \ \partial\theta/\partial X = 0 \quad \text{on } X = 1,\ \ 0 \leqslant Y \leqslant 1, \tag{10d}$$

Top adiabatic wall:

$$\psi = -D/H,\ \ \partial\theta/\partial Y = 0 \quad \text{on } Y = 1,\ \ D/H < X \leqslant 1, \tag{10e}$$

Outlet:

$$\partial\psi/\partial Y = 0,\ \ \partial\theta/\partial Y = 0 \quad \text{on } Y = 1,\ \ 0 \leqslant X \leqslant D/H. \tag{10f}$$

It should be noticed that the vertical velocity component, V, is numerically equal to unity at the inlet. Hence the stream-function value at the inlet can be obtained by integrating V from Eq. (6) with respect to X between the limits 0 and D/H. This gives the boundary condition (10b) for ψ. The three adiabatic surfaces of the cavity are connected together, and hence they all have the same constant value of $\psi = -D/H$. For the inlet flow, the temperature is known and it is set numerically equal to zero. The assumptions of outlet boundary condition is not easy. Convection is assumed to be dominant in the outflow through the vent. The conduction through the outlet will then be almost negligible. Hence the temperature gradient ($\partial T/\partial y$) is assumed to be zero at the outlet. Several authors used such a boundary condition for the energy equation at the outlet boundary; for example, Prasad et al. [24] for porous media and Angirasa [14] for non-porous media. It is seen that Eqs. (7) and (8) subject to the boundary conditions (10) involve three parameters, namely, Ra, Pe, and D/H. The relative magnitude of the Rayleigh and Péclet numbers determine which of the two mechanisms of forced or free convection flow is predominant.

The physical quantities of interest in this problem are the local Nusselt number along the hot wall, which is defined by

$$Nu_{\mathrm{L}} = -\left(\frac{\partial\theta}{\partial X}\right)_{X=0} \tag{11}$$

and also the average Nusselt number along the hot wall defined as

$$Nu_{\mathrm{av}} = \int_0^1 Nu\,\mathrm{d}Y. \tag{12}$$

3. Numerical method

We developed a computer code (NATURE, written in FORTRAN 77) in order to solve the governing equations. NATURE is a finite volume code, but is based on a finite element approach of representing the geometry. The finite volume method proceeds by integrating Eqs. (7) and (8) over a fixed control volume, which, using Gauss's theorem, result in

$$\int_s \frac{\partial\psi}{\partial X}\,\mathrm{d}n_x + \int_s \frac{\partial\psi}{\partial Y}\,\mathrm{d}n_y = \int_v \frac{Ra}{Pe}\frac{\partial\theta}{\partial X}\,\mathrm{d}v, \tag{13}$$

$$\int_v \frac{\partial\theta}{\partial\tau}\,\mathrm{d}v + \int_s u\theta\,\mathrm{d}n_x + \int_s v\theta\,\mathrm{d}n_y = \int_s \frac{\partial\theta}{\partial X}\,\mathrm{d}n_x + \int_s \frac{\partial\theta}{\partial Y}\,\mathrm{d}n_y, \tag{14}$$

where "v" and "s" denote volume and surface integrals, respectively, and $\mathrm{d}n_x$ and $\mathrm{d}n_y$ are the differential Cartesian components of the outward normal surface vector. The

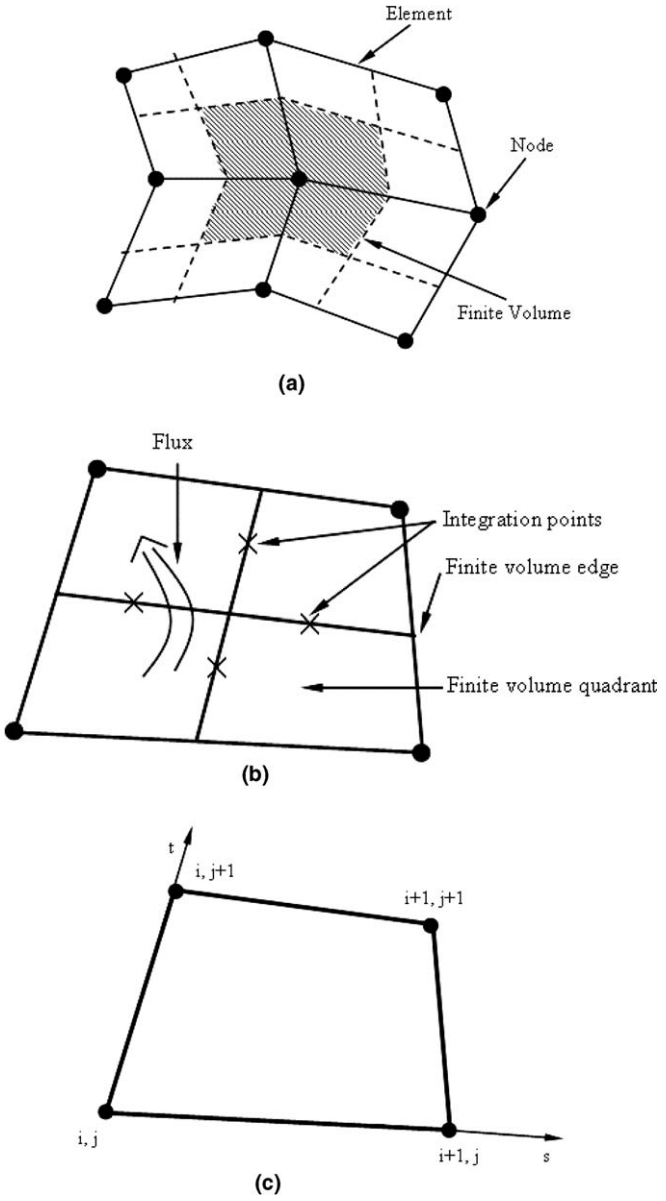

Fig. 2. (a) The definition of the control volume, (b) integration point definition for a 2-D quadrilateral element, and (c) four noded flux element.

surface integrals are integrations of the fluxes of the conserved quantities, whereas the volume integrals represent source terms. What defines the control volume is an important distinguishing feature of finite volume implementations. The computational domain is discretized into elements. Then control volume surfaces are defined by element mid-planes. This approach has been used by other researchers, for example, Schneider and Raw [25,26]. The procedure creates a control volume for each node, with the boundary of each interior control volume defined by eight line-segments in 2-D. This arrangement is shown in Fig. 2a. The integral equations, Eqs. (13) and (14), are applied to each discrete control volume created by this technique. The continuous volume integrations are relatively easy to convert to a discrete form, as will be shown later. The continuous surface integrations are more involved and are converted to a discrete form by evaluating them at *integration point*s (*ip*). The location of the integration points for one flux element is shown in Fig. 2b for a 2-D quadrilateral element. The surface fluxes must be discretely represented at the integration points to complete the conversion of the continuous equations to their discrete counterparts. The discrete form of the integral equations are written as

$$\sum_{ip}\left(\frac{\partial\psi}{\partial X}\Delta n_x\right)_{ip}+\sum_{ip}\left(\frac{\partial\psi}{\partial Y}\Delta n_y\right)_{ip}-\overline{\frac{Ra}{Pe}\frac{\partial\theta}{\partial X}}\mathrm{Vol}=0 \qquad (15)$$

and

$$\mathrm{Vol}\left(\frac{\theta-\theta^0}{\Delta\tau}\right)+\sum_{ip}(u\Delta n_x)^0_{ip}\theta_{ip}+\sum_{ip}(v\Delta n_y)^0_{ip}\theta_{ip}-\sum_{ip}\left(\frac{\partial\theta}{\partial X}\Delta n_x\right)_{ip}-\sum_{ip}\left(\frac{\partial\theta}{\partial Y}\Delta n_y\right)_{ip}=0, \qquad (16)$$

where "Vol" is the volume of the control volume, the subscript "*ip*" denotes an integration point, the summation is over all the integration points of the surface, Δn_x and Δn_y are the discrete outward surface vectors, Δt is the time step, the superscript "0" means "at the old time level", and the overbar on the source terms indicate an average value for the control volume.

The time step term,

$$\mathrm{Vol}\left(\frac{\theta-\theta^0}{\Delta\tau}\right) \qquad (17)$$

Table 1a
Comparison of the average Nusselt number for a closed cavity with some previous numerical results

Authors	Nu_{av}		
	$Ra=10$	$Ra=100$	$Ra=1000$
Mahmud and Fraser [30]	1.079	3.14	13.82
Walker and Homsy [31]	–	3.10	12.96
Gross et al. [32]	–	3.14	13.45
Moya et al. [33]	1.065	2.80	–
Manole and Lage [34]	–	3.12	13.64
Baytas and Pop [35]	1.079	3.16	14.06
Saeid and Pop [36]	–	3.002	13.726
Present prediction	1.079	3.14	13.82

Table 1b
Average Nusselt number for $D/H=0.3$ and $Pe=10$ for the aiding flow situation at different grid sizes (N) and Rayleigh numbers (Ra)

Ra	Average Nusselt number (Nu_{av})				
	$N=5000$	$N=10{,}000$	$N=20{,}000$	$N=40{,}000$	$N=80{,}000$
10	2.851	2.446	2.384	2.380	2.380
100	2.562	2.311	2.238	2.236	2.236
250	2.365	2.015	1.922	1.917	1.917
500	2.015	1.720	1.652	1.624	1.624

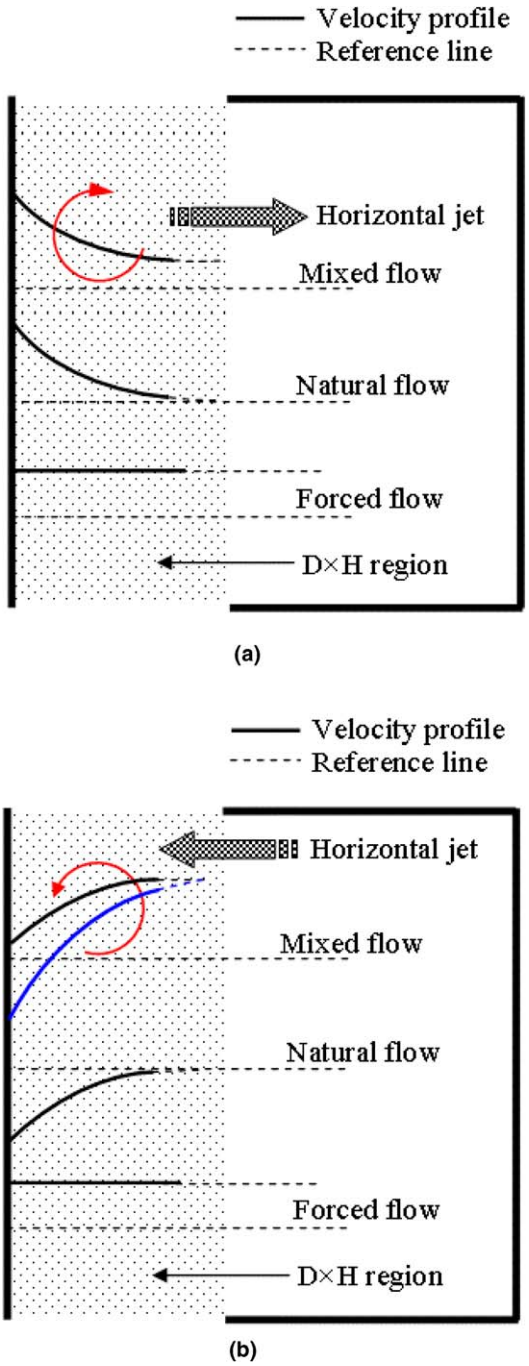

Fig. 3. (a) Schematic of velocity profiles at aiding flow situation and (b) schematic of velocity profiles at opposing flow situation.

is a first-order accurate backward Euler approximation to the transient term. It is also sometimes called the ''lumped mass'' approximation. It is robust, is fully implicit so it creates no time step limitation and is easy to implement.

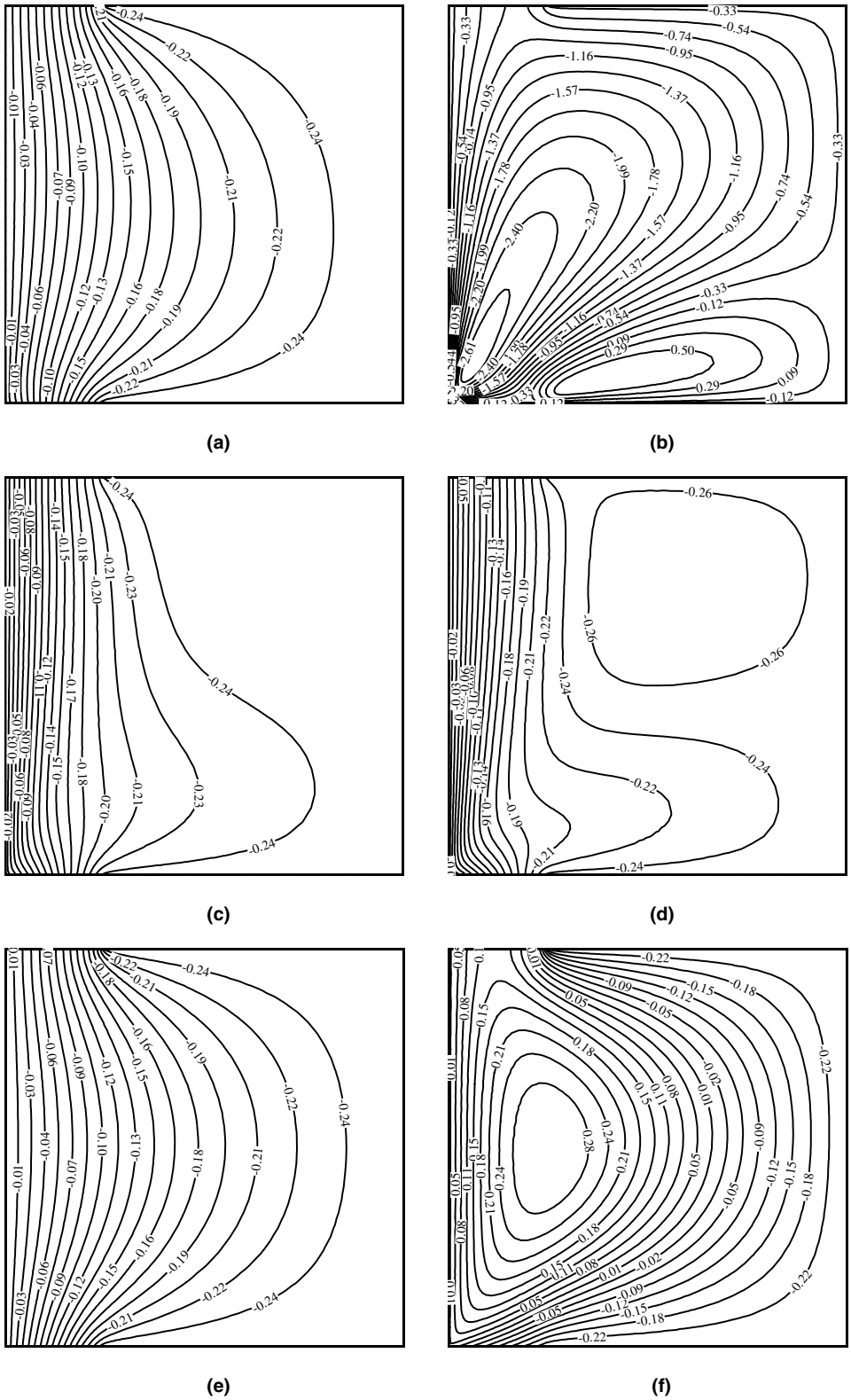

Fig. 4. Streamline for (a) aiding flow: $D/H = 0.25$, $Pe = 1$, $Ra = 1$; (b) aiding flow: $D/H = 0.25$, $Pe = 1$, $Ra = 500$; (c) aiding flow: $D/H = 0.25$, $Pe = 20$, $Ra = 50$; (d) aiding flow: $D/H = 0.25$, $Pe = 10$, $Ra = 50$; (e) opposing flow: $D/H = 0.25$, $Pe = 100$, $Ra = 1$; and (f) opposing flow: $D/H = 0.25$, $Pe = 5$, $Ra = 50$.

However, this does mean that transient calculations are only first-order accurate in time. As it should, this term has no bearing on the steady-state solution.

Following the standard finite element approach, shape functions are used to evaluate the derivatives for all the diffusion terms. For instance, for a derivative in the "x" direction at integration point "ip",

$$\left.\frac{\partial \Phi}{\partial X}\right|_{ip} = \sum_n \left.\frac{\partial N_n}{\partial X}\right|_{ip} \Phi_n, \tag{18}$$

where the summation is over all the shape functions for the element. In Eq. (18), Φ represents any variable, for example, Θ, ψ, etc. The Cartesian derivatives of the shape functions can be expressed in terms of their local derivatives via the Jacobian transformation matrix,

$$\begin{pmatrix} \frac{\partial N}{\partial X} \\ \frac{\partial N}{\partial Y} \end{pmatrix} = \begin{pmatrix} \frac{\partial X}{\partial s} & \frac{\partial Y}{\partial s} \\ \frac{\partial X}{\partial t} & \frac{\partial Y}{\partial t} \end{pmatrix}^{-1} \begin{pmatrix} \frac{\partial N}{\partial s} \\ \frac{\partial N}{\partial t} \end{pmatrix}. \tag{19}$$

For the (i,j) flux element (see Fig. 2c) the domain of the element can be defined in terms of the local, non-orthogonal coordinates s and t by

$$\begin{aligned} X(s,t) &= N_1 X_{i,j} + N_2 X_{i+1,j} + N_3 X_{i,j+1} + N_4 X_{i+1,j+1}, \\ Y(s,t) &= N_1 Y_{i,j} + N_2 Y_{i+1,j} + N_3 Y_{i,j+1} + N_4 Y_{i+1,j+1}, \end{aligned} \tag{20}$$

where the shape functions N are given by

$$\begin{aligned} N_1 &= \frac{1}{4}(1-s)(1-t), \quad N_2 = \frac{1}{4}(1+s)(1-t), \\ N_3 &= \frac{1}{4}(1-s)(1+t), \quad N_4 = \frac{1}{4}(1+s)(1+t). \end{aligned} \tag{21}$$

In order to discretize the advection terms, a modified central differencing scheme is used. This method uses upwind differencing scheme (UDS) with a correction as shown in the following equation:

$$\Phi_{ip} = \Phi_{up} + (\Delta\Phi_{ip})^0 \quad \text{with } \Delta\Phi_{ip} \approx \frac{\Delta X}{2}\left(\frac{\partial \Phi}{\partial X}\right)_{ip}, \tag{22}$$

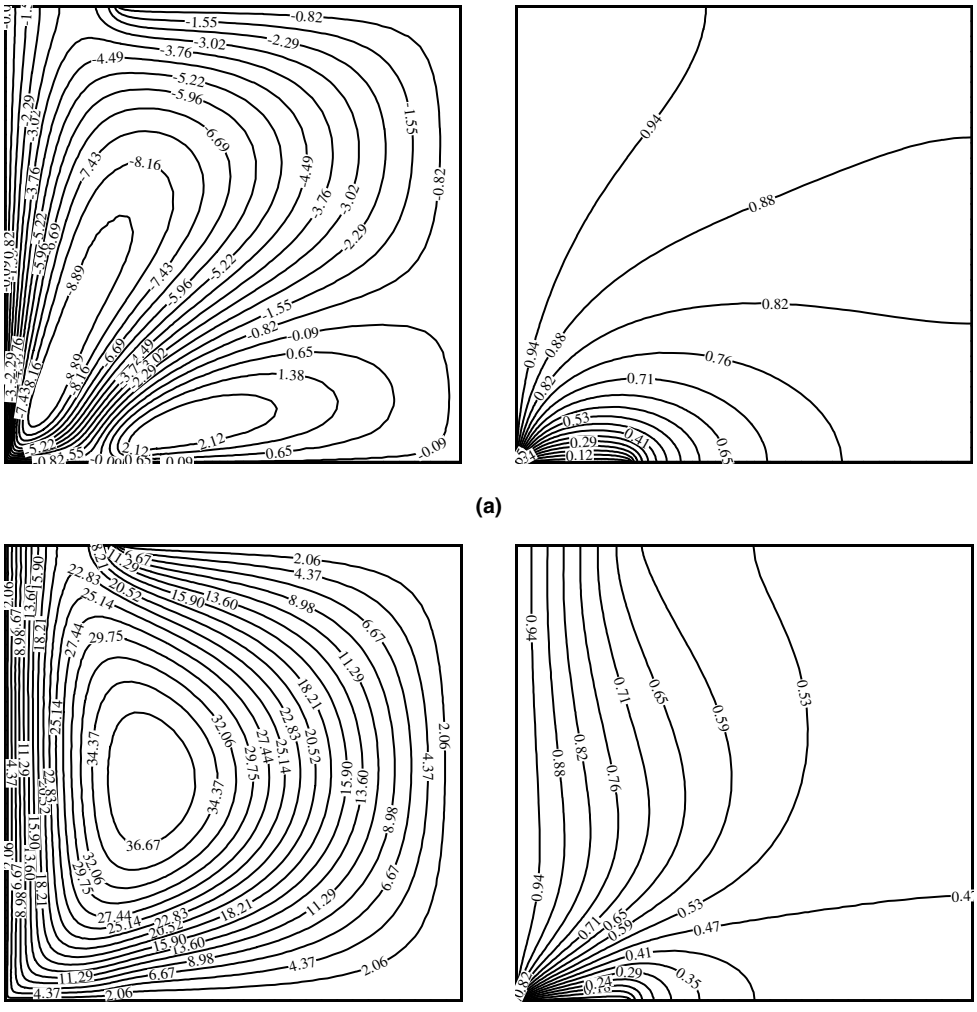

Fig. 5. Streamlines (left) and isotherms (right) for $Pe = 0.1$, $Ra = 100$ and $D/H = 0.25$: (a) aiding flow and (b) opposing flow.

which shows the approximation of Φ_{ip} for the x-direction only. The approximation of the source term is shown in Das et al. [27] and is not repeated here. After summing up all cell face fluxes and sources, the discretized transport equation reduces to the following algebraic equation:

$$A_P\Phi_P + \sum_{nb} A_{nb}\Phi_{nb} = Q_\Phi, \tag{23}$$

where the coefficient A_{nb}, contains the convective and diffusive flux contribution and Q_Φ represents the source term. The system of equations is solved by using TDMA (tri-diagonal matrix algorithm) solver [28]. The whole computational domain is subdivided on an unequally spaced control volumes. The time increment ($\Delta\tau$) was 10^{-4} in most of the cases; but sometimes, especially at high $|Ra|$ smaller values were chosen in order to confirm the accuracy of the results.

4. Accuracy and validation

The current numerical technique was very successfully used in a series of recent papers; for example, Mahmud et al. [29], and Mahmud and Fraser [30]. The values of the average Nusselt number, given by Eq. (12), along the left vertical wall of a classical porous square cavity (a porous cavity with two differentially heated vertical isothermal walls and two adiabatic horizontal walls and the porous media obeying the Darcy's law) for several values of the Rayleigh number are compared with those reported by Mahmud and Fraser [30], Walker and Homsy [31], Gross et al. [32], Moya et al. [33], Manole and Lage [34], Baytas and Pop [35], and Saeid and Pop [36]. It is seen that the present results are in very good agreement with those reported by these authors (see Table 1a). Therefore, these comparisons support very well the validity of the present computations. Table 1b shows the variation of average Nusselt number as a function of grid sizes (N) and Rayleigh numbers (Ra) for $D/H = 0.3$ and $Pe = 10$. Results of Nu_{av} are reported up to three decimal places. It is observed in Table 1b that the values of Nu_{av} for all the selected cases are for same $N = 40{,}000$ and $N = 80{,}000$. For better accuracy, $N = 80{,}000$ is selected to present the results in this paper.

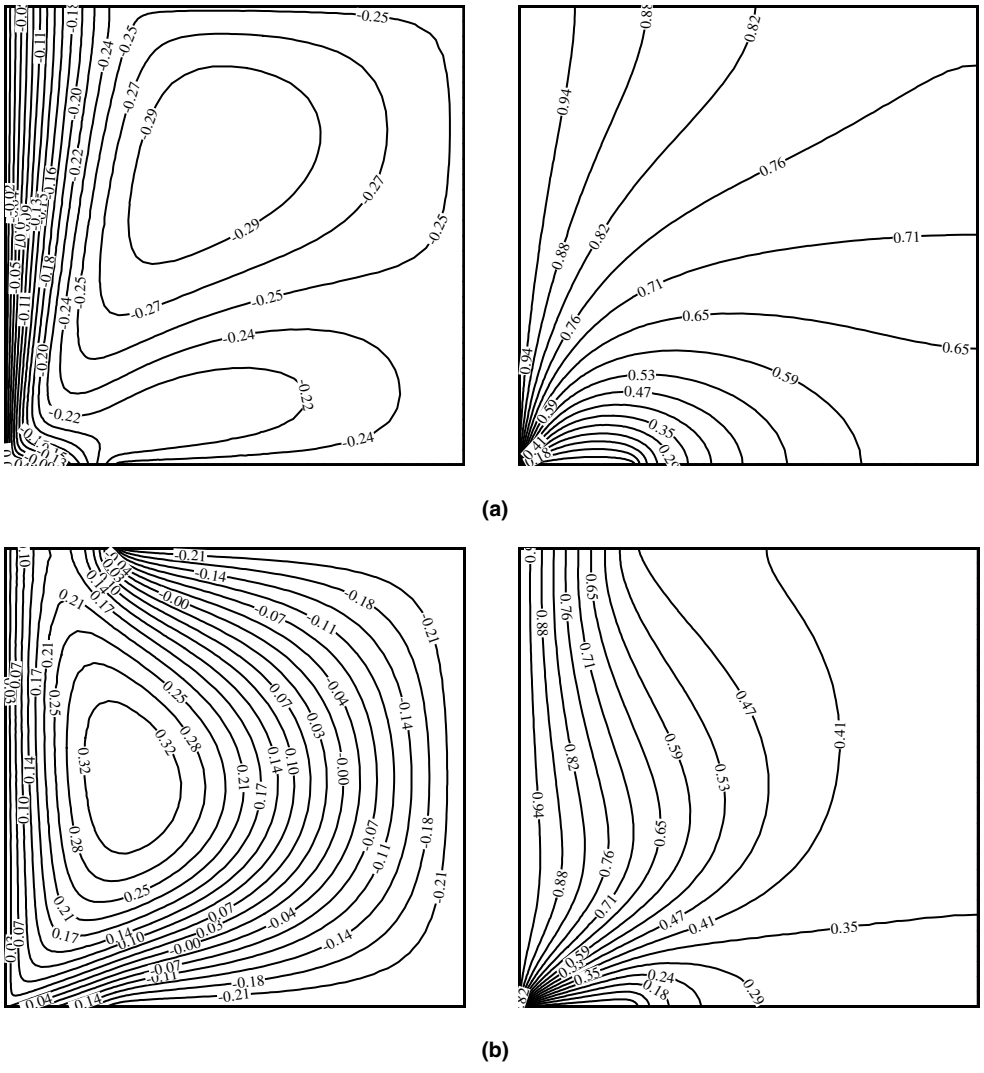

Fig. 6. Streamlines (left) and isotherms (right) for $Pe = 10$, $Ra = 100$ and $D/H = 0.25$: (a) aiding flow and (b) opposing flow.

5. Results and discussion

5.1. Flow and thermal fields

The mechanism of flow inside the enclosure can be well understood if one considers a simplified forced flow and a natural flow (buoyancy induced) separately. The discussion is first restricted to the aiding flow situation. Consider the case of a forced flow with uniform inlet velocity of V_0. Fig. 3a is helpful for understanding the following discussions. The velocity boundary layer thickness is not encountered in the vicinity of the isothermal wall because of the consideration of negligible pore Reynolds number in Darcy model; that is, $V_0\sqrt{K}/\nu \ll 1$ (see [37]). The wall friction effect is not felt beyond a few pore lengths $\sqrt{K}$ in the y direction. In other words, the hydrodynamic boundary layer thickness is so small that one can neglect it and consider the flow situation as inviscid. In such a case, the v-velocity profile is a horizontal line (see Fig. 3a) and its magnitude equals V_0. One can perform a simple scale analysis (see Bejan [37], and Mahmud and Fraser [30] for details) on Eqs. (3) and (7) in order to obtain $\psi \sim C_1 x$ where C_1 is an arbitrary constant. As the inlet temperature (T_0) of the fluid is different from the isothermal wall temperature (T_w) a thermal boundary layer (δ_T) must exist. The thickness of the thermal boundary layer can be calculated by considering another scale analysis on Eqs. (4) and (8) which results in $\delta_T \sim yPe_y^{-1/2}$ where Pe_y is the Péclet number based on the length y. Now, consider the case of the natural or buoyancy induced flow. The effect of buoyancy is strong near the vertical isothermal wall. Due to the negligible pore Reynolds number, the maximum v-velocity occurs after a few pore lengths $\sqrt{K}$ from the wall. The v-velocity (see Fig. 3a) will decrease to zero with increasing horizontal distance similar to that seen in the classical buoyancy induced boundary layer flow near a vertical wall (see [37]). Performing again a scale analysis on Eqs. (4) and (8), it is possible to show that for a natural flow $\delta_T \sim yRa_y^{-1/2}$ where Ra_y is the Rayleigh number based on the length y. For simplicity, if one considers the mixed

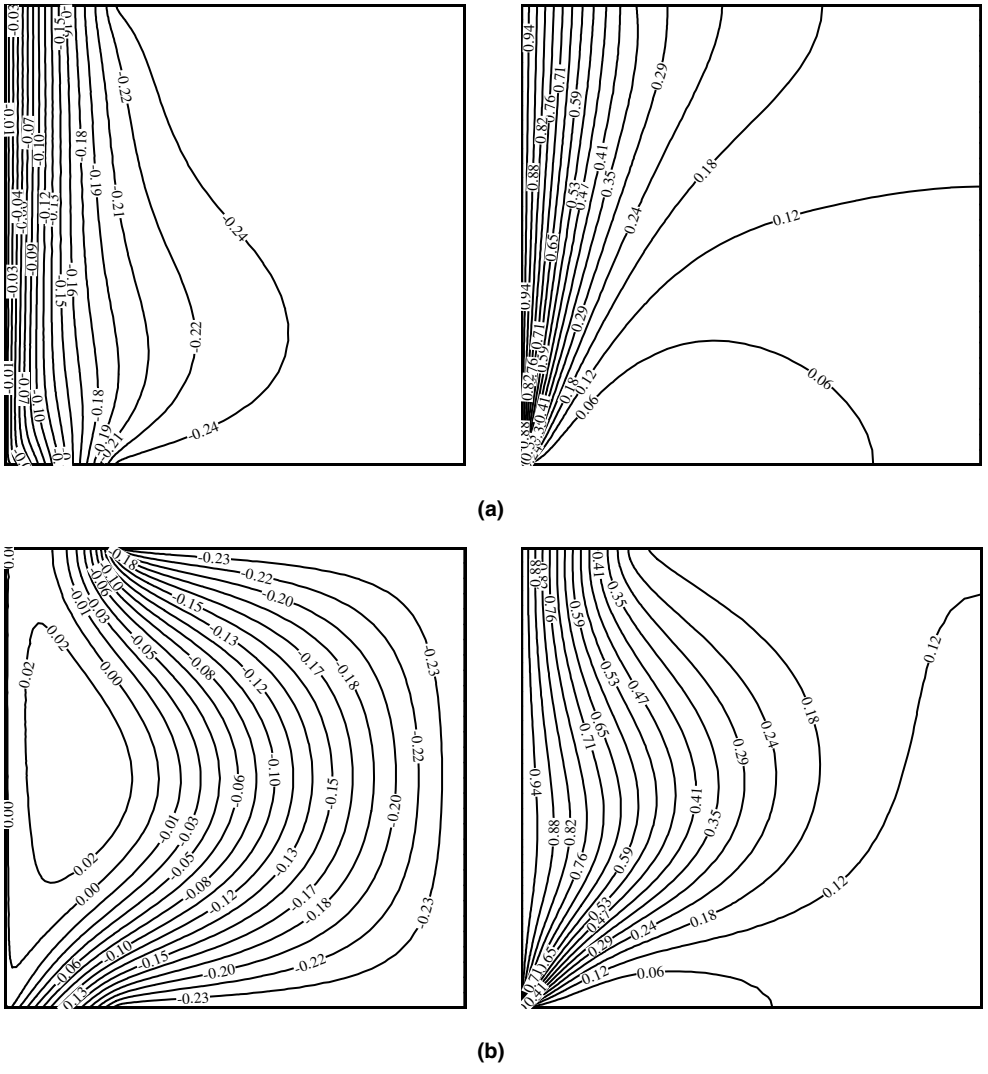

Fig. 7. Streamlines (left) and isotherms (right) for $Pe = 50$, $Ra = 100$ and $D/H = 0.25$: (a) aiding flow and (b) opposing flow.

convection flow as a superposition of the forced flow and the natural flow (see Fig. 3a), there exist non-zero vorticity components inside the region occupied by the area $D \times H$ just after the isothermal wall which is responsible for a horizontal stream of jet. Streamlines are no-longer parallel to the isothermal wall (see Fig. 4a) as is the case of a forced flow. Note that the strength of the vorticity is proportional to the temperature gradient $\partial T/\partial x$ and, in the absence of $\partial T/\partial x$, current problem reduces to a forced flow problem. The particular streamline, originated at the right edge of the inlet ($\psi = -0.25$, not shown in Fig. 4a) represents three adiabatic walls. The streamline $\psi = -0.24$ makes a void region with the three adiabatic walls where fluid is almost motionless. An increasing forced flow or natural flow change the flow pattern inside the enclosure. The simplified model presented above may not be suitable to describe the flow pattern in such a situation. A comparatively high buoyancy force strengthens the near wall vorticity as well as the horizontal stream which pushes the parameter $\psi = -0.24$ further to the adiabatic walls (see Fig. 4b). Due to the convective current, the secondary flow appears just over the bottom wall. The egg-shaped primary circulation bubble originates due to the strong vorticity in the $D \times H$ region near the isothermal wall as discussed earlier (as given by Fig. 3).

A strong forced flow can cause a flow separation from the right edge of the inlet. Combinations of strong forced flow and week natural flow can cause an almost horizontal mixed flow profile thus weakening the strength of vorticity in the $D \times H$ region. An example of such a case is depicted in Fig. 4c. A major portion of the streamlines from inlet to the exit vent appears to be straight (parallel to the isothermal wall) and nearly unperturbed by the buoyancy force. There is no indication of circulating bubble. The reduction of the strength of the forced flow of Fig. 4c introduces a circulating bubble as shown in Fig. 4d due to the stronger horizontal jet.

In contrast, the opposing flow situation can produce two different types of mixed flow profiles as shown in Fig. 3b depending on the relative magnitude of the forced flow velocity and natural flow velocity. It should be noted that the natural velocity is negative in the opposing flow case.

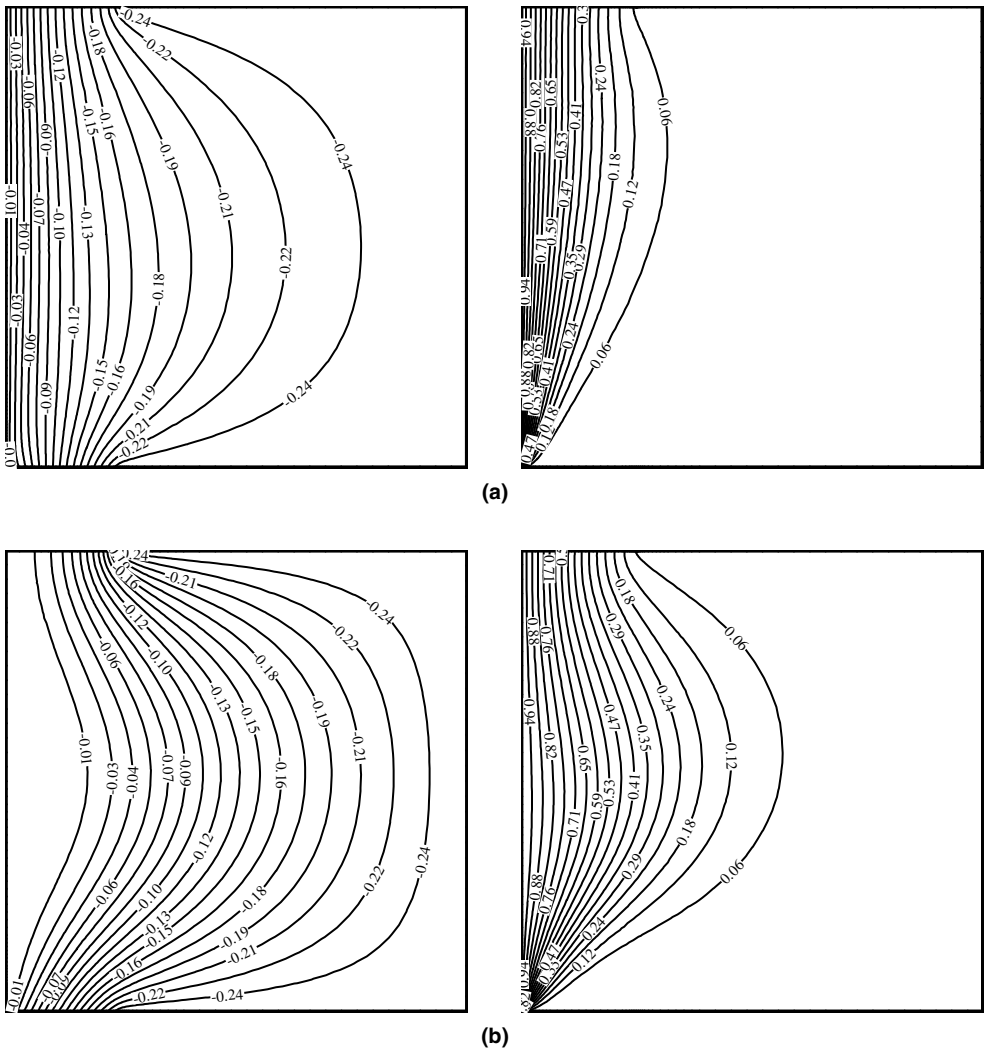

Fig. 8. Streamlines (left) and isotherms (right) for $Pe = 100$, $Ra = 100$ and $D/H = 0.25$: (a) aiding flow and (b) opposing flow.

For a strong enough forced velocity (see Fig. 4e), mixed velocity profile is positive everywhere and nearly horizontal that causes a weaker horizontal jet. However, for a strong enough natural velocity, a part of mixed velocity is negative

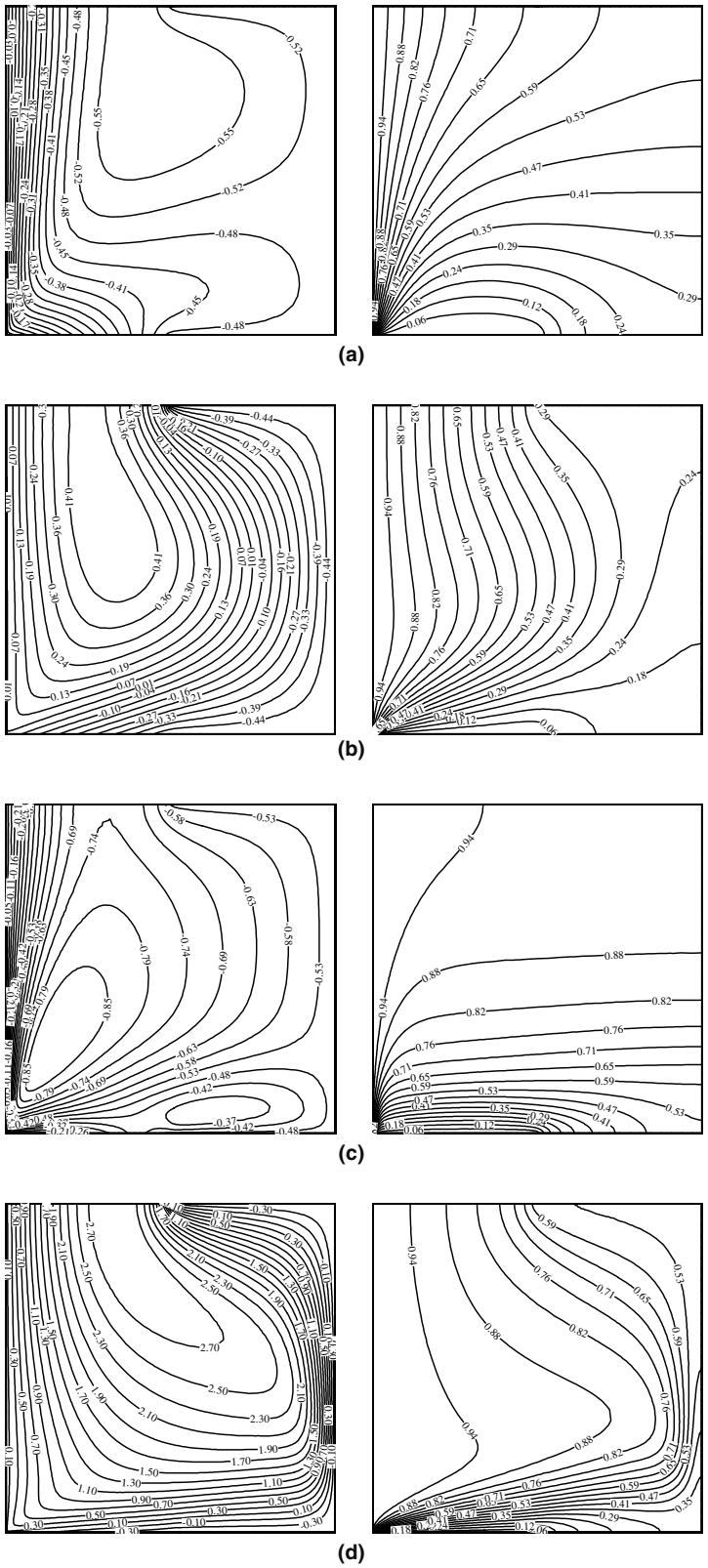

Fig. 9. Streamlines (left) and isotherms (right) for $Pe = 10$, $Ra = 100$ and $D/H = 0.5$: (a) aiding flow and (b) opposing flow. For $Pe = 10$, $Ra = 1000$ and $D/H = 0.5$: (c) aiding flow and (d) opposing flow.

and another part is positive as shown in Fig. 3b. An example case of such a situation is depicted in Fig. 4f. The downward moving fluid near the isothermal wall and the upward moving fluid from the inlet through the right portion of the enclosure to the exit vent create a large recirculation bubble.

Streamlines and isotherms contours are plotted in Figs. 5–10 for both aiding and opposing flow cases. The results in Figs. 5 and 6 are for $D/H = 0.25$, $Ra = 100$ and $Pe = 0.1$ and 10, which correspond to the case when the heat transfer inside the cavity is dominated by conduction mode. As Ra increases ($Ra = 100$, for example), the convection heat transfer becomes the dominant heat transfer mode. It is noticed a primary circulation zone with streamlines close to the left vertical wall for the opposing flow case (Figs. 5b and 6b) and secondary circulation zones (Figs. 5a and 6a). For increasing Pe number ($Pe = 50$) there is a small circulation zone only for the case of opposing flow as seen in Fig. 7. The transformation of the unicellular pattern to multicellular pattern may be attributed to the enhancement of buoyancy force brought in by increasing

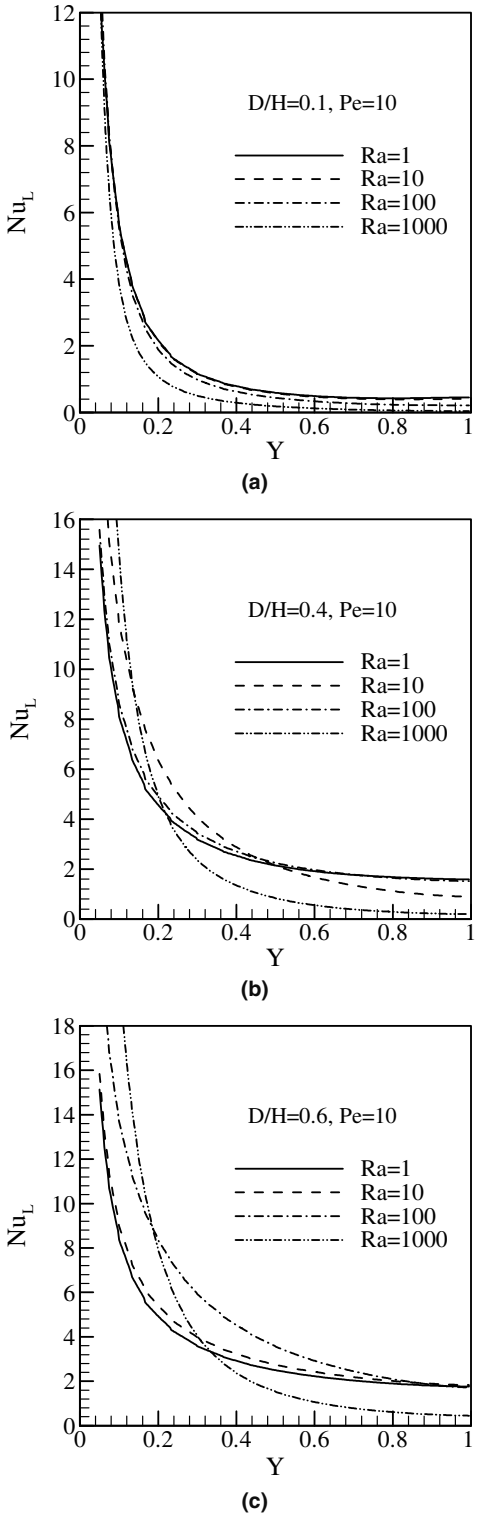

Fig. 10. Local Nusselt number at (a) $Pe = 10$, $D/H = 0.1$; (b) $Pe = 10$, $D/H = 0.4$; and (c) $Pe = 10$, $D/H = 0.6$.

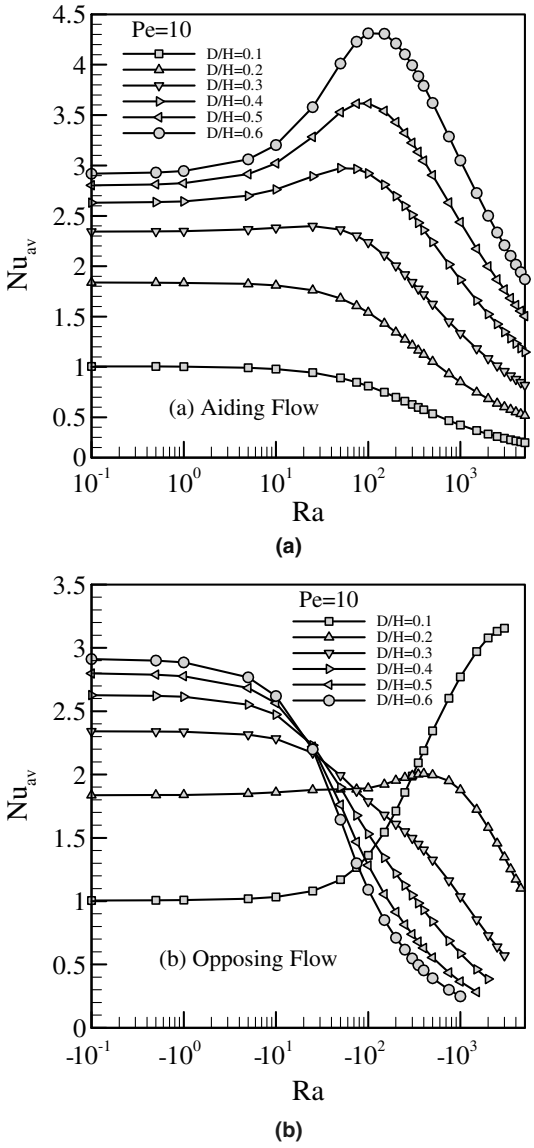

Fig. 11. Variation of the average Nusselt number with Ra for $Pe = 10$ and different values of D/H: (a) aiding flow and (b) opposing flow.

Ra. Secondary recirculation zones are known to hinder the heat transfer process. The results for isotherms in Fig. 9a–d show a stratified flow within the enclosure with steep gradients near the isothermal vertical wall. However, the temperature gradient increases near the isothermal vertical wall when both *Pe* and *Ra* are equal ($Pe = Ra = 100$) as seen in Fig. 8.

5.2. Local and global heat transfer

As $(T_w - T_0)$ is selected as a reference temperature difference for the current problem the local heat transfer rate from or to the isothermal wall entirely depends on the temperature gradient at that wall $(\partial T/\partial x|_{x=0})$ due to the fact that both T_w and T_0 are set constant. The lower left corner of the enclosure where the inlet and the isothermal wall intersect is always critical due to the singularity for the temperature gradient. To avoid the appearance of such a singularity, we start calculating the temperature gradient at a location of y slightly above $y = 0$. Fig. 10a–c show the local Nusselt number (Nu_L) distribution at some selected parameters mentioned in the plots. The region near the lower left corner of the enclosure is identified to show a thermal spot of high concentration of isotherms. Temperature gradient is higher in magnitude around this region. As one proceeds towards the exit vent along the isothermal wall, the isotherms are driven away from the isothermal wall due to the horizontal jet thus lowering the temperature gradient. For obvious reasons, Nu_L is high in magnitude at the lower left region of the enclosure and it decreases with increasing y as shown in Fig. 10a–c. Closer to the exit vent, isotherms inside the $D \times H$ region are nearly parallel to the isothermal wall due to the uniform horizontal jet. In this region, Nu_L are more or less independent of the vertical distance. When $D/H = 0.1$, the horizontal jet in the narrow $D \times H$ region is not strong enough to drive the isotherms far away from the left wall even at the high Rayleigh number ($Ra = 1000$). Consequently, the variation between the magnitudes of two consecutive Nu_L–y profiles are small; more specifically, at lower Rayleigh numbers as shown in Fig. 10a. When the line integration of Nu_L is performed to obtain the average Nusselt number (Nu_{av}) (see Fig. 11a) the variation of Nu_{av} with *Ra* is small when compared to the variation of Nu_{av} with *Ra* at high D/H. The Nu_L–y profiles at other *Ra* and D/H shows the similar distribution pattern whose reason is already described earlier but only change is observed in their relative magnitudes. Consider a case of a high D/H (for example, $D/H = 0.6$) keeping other parameters (*Pe*, *Ra*, etc.) constant. In such a situation the larger inlet will allow more forced flow which can cause the isotherms more concentrated to the left wall around the bottom left portion of the enclosure. For constant Péclet number and Rayleigh number, higher D/H shows larger Nu_L in general and the average Nusselt number increases with increasing D/H. There are also some exceptions; for example, at $D/H = 0.6$, the horizontal jet is strong enough at high Rayleigh number ($Ra = 1000$) to drive the isotherms far away from the left wall. The near

Table 2
Values of the average Nusselt number at different D/H: aiding flow situation for $Pe = 10$

Ra	Average Nusselt number (Nu_{av})					
	$D/H = 0.1$	$D/H = 0.2$	$D/H = 0.3$	$D/H = 0.4$	$D/H = 0.5$	$D/H = 0.6$
0.1	1.005	1.837	2.343	2.630	2.803	2.918
0.5	1.004	1.836	2.345	2.636	2.812	2.930
1	1.003	1.835	2.347	2.643	2.824	2.944
5	0.992	1.824	2.364	2.699	2.914	3.061
10	0.979	1.809	2.380	2.762	3.021	3.202
25	0.943	1.762	2.398	2.893	3.284	3.579
50	0.892	1.681	2.363	2.974	3.529	4.011
75	0.848	1.606	2.302	2.965	3.614	4.229
100	0.811	1.540	2.236	2.921	3.617	4.311
150	0.749	1.431	2.110	2.809	3.543	4.307
200	0.700	1.344	2.005	2.696	3.430	4.212
250	0.660	1.274	1.917	2.597	3.324	4.103
300	0.627	1.215	1.840	2.509	3.225	3.995
350	0.599	1.166	1.775	2.431	3.135	3.886
400	0.575	1.123	1.719	2.358	3.047	3.790
500	0.536	1.053	1.624	2.239	2.904	3.620
750	0.467	0.930	1.448	2.017	2.632	3.287
1000	0.423	0.851	1.334	1.865	2.438	3.050
1500	0.368	0.748	1.181	1.659	2.174	2.726
2000	0.333	0.684	1.083	1.524	1.999	2.501
2500	0.309	0.638	1.012	1.426	1.869	2.335
3000	0.291	0.603	0.957	1.346	1.768	2.207
3500	0.277	0.575	0.914	1.284	1.683	2.103
4000	0.265	0.553	0.877	1.232	1.615	2.016
4500	0.256	0.534	0.847	1.186	1.556	1.941
5000	0.248	0.517	0.819	1.148	1.505	1.870

wall isothermal lines in such a case become nearly horizontal to the bottom wall which causes a very low temperature gradient as well as low Nu_L relative to the Nu_L at low Rayleigh numbers. Average Nusselt number shows a decreasing tendency after getting a peak (see Fig. 11a) in such a situation.

Some values of the average Nusselt number, Nu_{av}, for different values of the parameters Pe, Ra and D/H are given in Tables 2–5 for both aiding and opposing flow cases. In addition, the variation of Nu_{av} with Ra is shown in Fig. 11 for $Pe = 10$ and the ratio D/H in the range from 0.1 to 0.6. It is interesting to note from Tables 2 and 3 that the global heat transfer into the enclosure is sensitive to the change of the parameter D/H and the reason behind this is already discussed in the previous paragraph. Thus, Nu_{av} increases with increasing this parameter for a fixed value of Pe (=10). For aiding flow Nu_{av} decreases monotonically for $D/H = 0.1$ and 0.2, while it has a maximum value for

Table 3
Values of the average Nusselt number at different D/H: opposing flow situation for $Pe = 10$

Ra	Average Nusselt number (Nu_{av})					
	$D/H = 0.1$	$D/H = 0.2$	$D/H = 0.3$	$D/H = 0.4$	$D/H = 0.5$	$D/H = 0.6$
−0.1	1.006	1.837	2.342	2.627	2.798	2.912
−0.5	1.007	1.838	2.340	2.622	2.789	2.900
−1	1.008	1.839	2.337	2.614	2.777	2.885
−5	1.019	1.849	2.315	2.553	2.683	2.767
−10	1.034	1.859	2.282	2.473	2.564	2.620
−25	1.080	1.878	2.170	2.231	2.220	2.198
−50	1.170	1.883	1.994	1.898	1.762	1.644
−75	1.266	1.884	1.869	1.677	1.469	1.300
−100	1.362	1.892	1.787	1.530	1.283	1.090
−150	1.545	1.922	1.681	1.343	1.056	0.851
−200	1.711	1.953	1.609	1.218	0.915	0.711
−250	1.859	1.976	1.550	1.123	0.815	0.617
−300	1.988	1.992	1.498	1.047	0.740	0.548
−350	2.093	2.002	1.450	0.984	0.680	0.495
−400	2.189	2.007	1.406	0.929	0.631	0.454
−500	2.345	1.997	1.326	0.840	0.555	0.392
−750	2.602	1.950	1.162	0.686	0.436	0.300
−1000	2.771	1.878	1.035	0.586	0.366	0.249
−1500	2.971	1.724	0.854	0.461	0.284	0.924
−2000	3.079	1.581	0.729	0.385	–	–
−2500	3.131	1.457	0.639	–	–	–
−3000	3.155	1.348	0.571	–	–	–

Table 4
Values of the average Nusselt number at different Péclet number: aiding flow situation for $D/H = 0.25$

Ra	Average Nusselt number (Nu_{av})						
	$Pe = 0.1$	$Pe = 1$	$Pe = 5$	$Pe = 10$	$Pe = 20$	$Pe = 50$	$Pe = 100$
1	1.134	1.223	1.632	2.126	2.923	4.415	6.055
50	1.007	1.086	1.476	2.033	3.205	5.483	7.146
100	0.923	0.995	1.355	1.891	3.156	6.358	8.205
500	0.678	0.724	0.962	1.332	2.313	6.781	13.423
1000	0.578	0.614	0.800	1.085	1.851	5.706	14.224
5000	0.401	0.421	0.519	0.664	1.037	2.952	9.186

Table 5
Values of the average Nusselt number at different Péclet number: opposing flow situation $D/H = 0.25$

Ra	Average Nusselt number (Nu_{av})						
	$Pe = 0.1$	$Pe = 1$	$Pe = 5$	$Pe = 10$	$Pe = 20$	$Pe = 50$	$Pe = 100$
−1	1.142	1.230	1.639	2.124	2.902	4.372	6.010
−50	1.363	1.435	1.709	1.981	2.414	3.432	4.943
−100	1.493	1.533	1.699	1.875	2.171	2.857	4.019
−500	1.515	1.528	1.586	1.652	1.763	1.982	2.234
−1000	1.337	1.343	1.372	1.404	1.458	1.552	1.638

$0.3 \leqslant D/H \leqslant 0.6$ and the considered value of Pe (=10). It is seen that the maximum value of Nu_{av} takes place for relatively low values of Ra between 10 and 150. On the other hand, for the opposing flow case, Nu_{av} increases monotonically with Ra for small values of D/H (=0.1, say) and decreases monotonically with Ra for $0.3 \leqslant D/H \leqslant 0.6$ but for $D/H = 0.2$ it has a maximum value for Ra in the range $350 \leqslant Ra \leqslant 500$. Further, Tables 4 and 5 show that Nu_{av} increases monotonically with increasing Pe, i.e., the forced convection flow for a fixed value of D/H (=0.25). In addition to this discussion it is also very important to notice from Tables 2–5 and Fig. 11 that for aiding flow case, solutions of Eqs. (7) and (8) can be obtained for all values of the parameters Pe, Ra and D/H considered. However, for opposing flow case, the solution diverges for all values of these parameters considered. Thus, for large negative values of Ra a combination of positive and negative mixed vertical velocity close to the left wall may cause a local circulation, instability, multiplicity, and even turbulent flow and the intensive study of such situations is beyond the scope of the present paper. Nevertheless, for some selected parameters, the following section performs a bifurcation analysis based on the concept of the *gradual run* and the *impulsive run* (see [38]). This is similar to the problem of mixed convection boundary layer flow over a vertical flat plate embedded in a porous medium where the boundary layer separation occurs for some values of the mixed convection parameter Ra/Pe. It is worth mentioning that the boundary layer separation in porous media has been first put in evidence by Merkin [39].

5.3. Bifurcation analysis

In this section, for some selected parameters ($D/H = 0.6$ and $Pe = 10$), we perform a special type of bifurcation analysis proposed by Wakitani [38] in order to check the existence of multiple solutions depending on the different initial conditions. To find out the dependency of the flow structure as well as the heat transfer rate on the initial condition, the numerical calculation is carried out either by an impulsive run or a gradual run. The numerical simulation in impulsive run starts by assuming a motionless isothermal initial state for each Rayleigh number. In contrast, the numerical simulation in gradual run is carried out by gradually increasing Rayleigh number where the initial condition during a simulation at a particular Rayleigh number is selected from previously solved converged solution at a lower Rayleigh number. For a comprehensive reference on such a bifurcation analysis, see articles by Wakitani [38,40]. The numerical solution so far presented in this paper is based on a gradual run. We re-simulate the special case of $D/H = 0.6$ and $Pe = 10$ for both aiding flow and opposing flow situations by using an impulsive run as stated earlier. The corresponding average Nusselt number as a function of Rayleigh number is presented in Fig. 12a. The previously obtained average Nusselt number (see Tables 2–4 and Fig. 11) from gradual run is also presented in Fig. 12a for a comparison purpose. As stated earlier, Nu_{av} shows a little or no variation with increasing Ra in the conduction dominated regime. The difference between the magnitudes of Nu_{av} at gradual run and impulsive run is very small (particularly in the conduction regime) and this is identified as single-branch (SB) solution as shown in Fig. 12a. The single-branch solution extends beyond the conduction regime to a point ($Ra \approx 50$ for aiding flow and $Ra \approx 25$ for opposing flow at $Pe = 10$ and $D/H = 0.6$) from where the multiple-branch (MB) solution is easily identifiable. In the MB region, Nu_{av} obtained by the impulsive run is lower in magnitude when compared with Nu_{av} obtained by the gradual run. The transition between the single-branch to multiple-branch solution (or

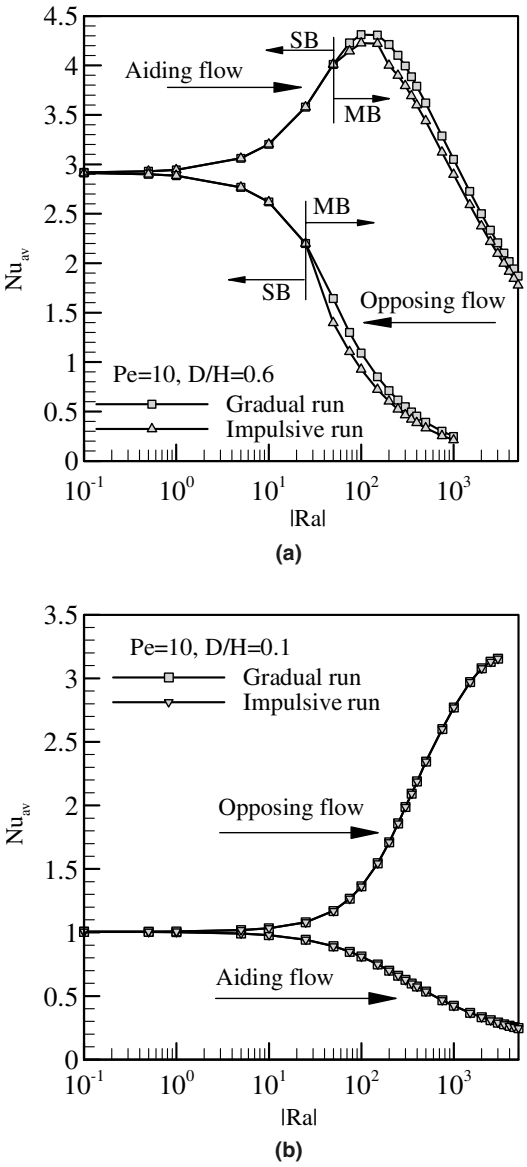

Fig. 12. Variation of average Nusselt number with Ra at (a) $Pe = 10$ and $D/H = 0.6$ and (b) $Pe = 10$ and $D/H = 0.1$ during gradual run and impulsive run (SB = single branch and MB = multiple branch).

multiple-branch to single-branch) is strictly governed by the existence of the convective motion and convective pattern change inside the enclosure (more specifically, in the $D \times H$ region) which is affected by change in the initial condition. In conduction regime, convective motion is negligible and a change in the initial condition shows a negligible effect in convective pattern change. Consequently, the average heat transfer rate is unaffected or little affected by the change in initial condition which results a single-branch solution. When convective motion starts at high Rayleigh number and becomes stronger, the gradual run solution slightly overpredicts the solution obtained by the impulsive run. If one is able to select an infinitely small gap between two consecutive Rayleigh numbers (which requires very large computational time) during gradual run the multiple-branch solution may theoretically become a single-branch solution. The step change from one steady-state solution at a low Ra to another steady-state solution at a high Ra creates an intermediate non-equilibrium situation that slightly changes the convective pattern (circulation bubble, strength of horizontal jet, etc.) in the enclosure. This change causes the multiple-branch solution as shown in Fig. 12a. The solution after the conduction regime and before the starting point of multiple-branch shows a single branch which requires an extensive investigation and leave for a future work. However, we could not identify any multiple-branch solution at low D/H; for example, $D/H = 0.1$ and $Pe = 10$ as shown in Fig. 12b.

6. Conclusions

Two-dimensional, steady mixed convection flow in a porous square vented cavity with an isothermal vertical surface and the other three walls being adiabatic has been studied numerically. The transformed equations of Darcy and energy in non-dimensional form have been solved numerically using the finite-volume method. Governing parameters chosen are Pe, Ra, and D/H which are varied in the ranges $0.1 \leqslant Pe \leqslant 100$, $0.1 \leqslant |Ra| \leqslant 1000$ and $0.1 \leqslant D/H \leqslant 0.6$. Both aiding and opposing buoyancies were considered. The obtained results showed that the parameter D/H considerably affects the flow and heat transfer characteristics in the cavity. Also, the variation of the parameters Pe, Ra, and D/H transform the flow pattern from a unicellular flow to a multicellular flow, especially, for small values of the forced flow (small values of Pe). It is shown that the global heat transfer into the enclosure is sensitive to the change of the parameter D/H for fixed values of the parameters Ra/Pe and Pe, respectively.

References

[1] D.A. Nield, A. Bejan, Convection in Porous Media, second ed., Springer, New York, 1999.

[2] D.B. Ingham, I. Pop (Eds.), Transport Phenomena in Porous Media, Pergamon, Oxford, 1998.

[3] D.B. Ingham, I. Pop (Eds.), Transport Phenomena in Porous Media, Pergamon, Oxford, 2002.

[4] D.B. Ingham, I. Pop (Eds.), Transport Phenomena in Porous Media, Elsevier, Oxford, 2005.

[5] K. Vafai (Ed.), Handbook of Porous Media, Marcel Dekker, New York, 2000.

[6] K. Vafai (Ed.), Handbook of Porous Media, second ed., Taylor & Francis, New York, 2005.

[7] I. Pop, D.B. Ingham, Convective Heat Transfer: Mathematical and Computational Modeling of Viscous Fluid and Porous Media, Pergamon, Oxford, 2001.

[8] A. Bejan, A.D. Kraus (Eds.), Heat Transfer Handbook, Wiley, New York, 2003.

[9] D.B. Ingham, A. Bejan, E. Mamut, I. Pop (Eds.), Emerging Technologies and Techniques in Porous Media, Kluwer, Dordrecht, 2004.

[10] A. Bejan, I. Dincer, S. Lorente, A.F. Miguel, A.H. Reis, Porous and Complex Flow Structures in Modern Technologies, Springer, New York, 2004.

[11] H. Hadim, K. Vafai, Overview of current computational studies of heat transfer in porous media and their applications—forced convection and multiphase heat transfer, in: W.J. Minkowycz, E.M. Sparrow (Eds.), Advances in Numerical Heat Transfer, vol. II, Taylor and Francis, New York, 2000, pp. 291–329.

[12] K. Vafai, H. Hadim, Overview of current computational studies of heat transfer in porous media and their applications—natural and mixed convection, in: W.J. Minkowycz, E.M. Sparrow (Eds.), Advances in Numerical Heat Transfer, vol. II, Taylor and Francis, New York, 2000, pp. 331–369.

[13] F.C. Lai, Mixed convection in saturated porous media, in: K. Vafai (Ed.), Handbook of Porous Media, Marcel Dekker, 2000, pp. 605–661.

[14] D. Angirasa, Mixed convection in a vented enclosure with an isothermal vertical surface, Fluid Dyn. Res. 26 (2000) 219–233.

[15] E. Holzbecher, Free convection in open-top enclosures filled with a porous medium heated from below, Numer. Heat Transfer (Part A) 46 (2004) 241–254.

[16] K. Khanafer, K. Vafai, Double-diffusive mixed convection in a lid-driven enclosure filled with a fluid-saturated porous medium, Numer. Heat Transfer (Part A) 42 (2002) 465–486.

[17] A.J. Chamkha, A.R.A. Khaled, Nonsimilar hydromagnetic simultaneous heat transfer by mixed convection from a vertical plate embedded in a uniform porous medium, Numer. Heat Transfer (Part A) 36 (1999) 327–344.

[18] A.J. Chamkha, Mixed convection flow along a vertical permeable plate embedded in a porous medium in the presence of transverse magnetic field, Numer. Heat Transfer (Part A) 34 (1998) 93–103.

[19] A.J. Chamkha, Non-Darcy fully developed mixed convection in a porous medium channel with heat generation/absorption and hydromagnetic effects, Numer. Heat Transfer (Part A) 32 (1997) 653–675.

[20] C.H. Chen, Non-Darcy mixed convection from a horizontal surface with variable surface heat flux in a porous medium, Numer. Heat Transfer (Part A) 30 (1996) 859–869.

[21] W.J. Chang, W.L. Chang, Mixed convection in a vertical tube partially filled with porous medium, Numer. Heat Transfer (Part A) 28 (1995) 739–754.

[22] T.K. Aldoss, M.A. Al-Nimr, M.A. Jarrah, B.J. Al-Sha'er, Magneto-hydrodynamic mixed convection from a vertical plate embedded in a porous medium, Numer. Heat Transfer (Part A) 28 (1995) 635–645.

[23] F.C. Chou, P.Y. Chung, Effect of stagnant conductivity on non-Darcian mixed convection in horizontal square packed channels, Numer. Heat Transfer (Part A) 27 (1995) 195–209.

[24] V. Prasad, F.C. Lai, F.A. Kulacki, Mixed convection in horizontal porous layers heated from below, J. Heat Transfer 110 (1988) 395–402.

[25] G.E. Schneider, M.J. Raw, A skewed, positive influence coefficient upwinding procedure for control-volume-based finite element convection–diffusion computations, Numer. Heat Transfer 8 (1986) 1–26.

[26] G.E. Schneider, M.J. Raw, Control-volume finite element method for heat transfer and fluid flow using collocated variables—1. Computational procedure, Numer. Heat Transfer 11 (1987) 363–390.
[27] P.K. Das, S. Mahmud, S.H. Tasnim, A.K.M.S. Islam, Effect of surface waviness and aspect ratio on heat transfer inside a wavy enclosure, Int. J. Numer. Methods Heat Fluid Flow 13 (2003) 1097–1122.
[28] J.H. Ferziger, M. Perić, Computational Methods for Fluid Dynamics, Springer, New York, 1996.
[29] S. Mahmud, P.K. Das, N. Hyder, A.K.M.S. Islam, Free convection in an enclosure with vertical wavy walls, Int. J. Thermal Sci. 41 (2002) 440–446.
[30] S. Mahmud, R.A. Fraser, Magnetohydrodynamic free convection and entropy generation in a square porous cavity, Int. J. Heat Mass Transfer 47 (2004) 3245–3256.
[31] K.L. Walker, G.M. Homsy, Convection in a porous cavity, J. Fluid Mech. 87 (1978) 449–474.
[32] R.J. Gross, M.R. Bear, C.E. Hickox, The application of flux-corrected transport (FCT) to high Rayleigh number natural convection in porous media, in: Proc. 8th Int. Heat Transfer Conference, San Francisco, CA, 1986.
[33] S.L. Moya, E. Ramos, M. Sen, Numerical study of natural convection in a tilted rectangular porous material, Int. J. Heat Mass Transfer 30 (1987) 741–756.
[34] D.M. Manole, J.L. Lage, Numerical benchmark results for natural convection in a porous medium cavity, HTD, vol. 216, Heat and Mass Transfer in Porous Media, ASME Conference, 1992, pp. 55–60.
[35] A.C. Baytas, I. Pop, Free convection in oblique enclosures filled with a porous medium, Int. J. Heat Mass Transfer 42 (1999) 1047–1057.
[36] N.H. Saeid, I. Pop, Transient free convection in a square cavity filled with a porous medium, Int. J. Heat Mass Transfer 47 (2004) 1917–1924.
[37] A. Bejan, Convection Heat Transfer, Wiley, New York, 1984.
[38] S. Wakitani, Development of multicellular solutions in natural convection in an air-filled vertical cavity, J. Heat Transfer 119 (1997) 97–101.
[39] J.H. Merkin, Mixed convection boundary layer flow on a vertical surface in a saturated porous medium, J. Eng. Math. 14 (1980) 301–313.
[40] S. Wakitani, Formation of cells in natural convection in a vertical slot at large Prandtl number, J. Fluid Mech. 314 (1996) 299–314.